Gravity currents produced by lock-release: theory and experiments concerning the effect of a free top in non-Boussinesq systems

S. Longo[a], M. Ungarish[b], V. Di Federico[c], L. Chiapponi[a], D. Petrolo[a]

[a]*Dipartimento di Ingegneria e Architettura (DIA), Università di Parma, Parco Area delle Scienze, 181/A, 43124 Parma, Italy*
[b]*Department of Computer Science, Technion, Israel Institute of Technology, Haifa 32000, Israel*
[c]*Dipartimento di Ingegneria Civile, Chimica, Ambientale e dei Materiali (DICAM), Università di Bologna, Viale Risorgimento, 2, 40136 Bologna, Italy*

Abstract

We present an experimental and theoretical analysis of non-Boussinesq iner-
tial gravity currents (GCs) flowing in rectangular cross-sections. Attention is
focused on the effects of the open upper boundary, which become pronounced
when the density contrast between the current and the ambient is significant
(non-Boussinesq case). The study is conducted deriving first a two-layer
shallow-water (SW) model for the release of a constant fluid volume into an
ambient of given height with a free-surface boundary condition, with an arbi-
trary density ratio r between the ambient and the intruding fluid. The jump
conditions at the front are provided by the novel extension of Benjamin's
(1968) [1] analysis , subject to energy-dissipation and sub-critical speed re-
quests, as detailed in Ungarish, (2017) [2]. The resulting SW lock-release
problem is solved via a finite difference approach. Lock-release experiments
are then conducted in this configuration with $r = 0.837 - 0.950$ and two dif-
ferent lock lengths. Experimental results obtained for the front position and
speed of the intruding current, its thickness, and the free-surface depression
of the ambient fluid (a signature of these experiments marking the position
of the intruding front) agree, to various degrees, with their theoretical coun-
terparts, with a better agreement for the front position and depression than
for the other quantities, but demonstrating in all cases the consistency of
the trend. Some of the experiments were repeated with a top-lid boundary
condition, to discern its effect on the current propagation. These effects turn

out to be relatively minor except for the obvious absence of interface-height depression. The range of density ratio r examined is further extended by conducting a numerical simulations with $r = 0.7$ using a numerical commercial Computational Fluid Dynamics code (CFD) based on Reynolds Averaged Navier-Stokes equations (RANS). A comparison among SW theory, experiments, and the numerical simulations is conducted in terms of the trough behind the current nose, leading to an overestimation of theoretical results with respect to experiments. The length of the through appreciably scales with the lock-length.

1. Introduction

Classical models of gravity currents (GCs) typically envisage a GC produced by lock-release advancing in an ambient fluid while the two-fluid system is contained from above by a fixed boundary (see Ungarish, 2009 [3] and the references therein). In most analyses the density of the current ρ_1 is slightly different from the ambient fluid's ρ_2, hence the ratio $r = \rho_2/\rho_1 \approx 1$. This is the Boussinesq case whereas the condition $r < 0.9$ is defined as the non-Boussinesq case. The lock-exchange with a fixed top in non-Boussinesq conditions has been studied experimentally, numerically and analitically [4, 5, 6, 7, 8, 9, 10, 11, 12, 13, 14, 15]. We emphasize that these studies are relevant to systems with a fixed-top boundary. However, in several real cases and especially in natural environments, GCs develop in an ambient fluid with a free surface, often in the presence of free surface waves [see, e.g., 16, 17] or of an imposed or generated flux [18, 19].

The effect of the open boundary on the motion of the lock-released (or lock-exchange) GC is a relatively uninvestigated topic. The presence of the open surface introduces a significant complication in the analysis of the GC, because the height of the upper boundary is now a variable of distance x and time t, which must be calculated (or measured in the laboratory). Moreover, the deviation from the fixed-top case turns out to be proportional to $(1 - r)$, and hence a reliable investigation must cover the more complex non-Boussinesq regime. This lack of knowledge has motivated the present investigation. The present paper attempts to clarify, and model, some salient effects of the GC system with an open surface.

2

The progress in the understanding of the GC with fixed top has been strongly facilitated by the availability of the classical Benjamin (1968) solution which is valid for both Boussinesq and non-Boussinesq systems with fixed top. Benjamin's speed and dissipation formulas serve as essential components in shallow-water models and in the interpretation of simulation and laboratory data. On the other hand, no counterpart solution was available for the free-surface systems until recently.

A recent paper by Ungarish, (2017) [2] has demonstrated that the classical Benjamin (1968) [1] solution can be extended to solve the free surface case, with a new front condition. Qualitatively, the open-surface problem introduces a decrease effect, or depression, χ in the height of the ambient fluid H, as a footprint of the advancing nose of the current. Since the ratio χ/H is proportional to $\Delta\rho/\rho_2$, ($\Delta\rho = \rho_1 - \rho_2$), in Boussinesq conditions the effect is modest and usually neglected. For non-Boussinesq conditions, the depression can be relevant and, to higher orders, interferes with the GC front speed and height. Experimental data for open surface systems are available, but only for Boussinesq systems, with the exception of very recent experiments reported in Sciortino et $al.$, (2018) [20]. On the other hand, most of the shallow water (SW) two-layer results are for covered channel (for the one-layer, very deep current, the presence/absence of the cover is insignificant). Some SW two-layer open-surface results have been presented by Adduce et $al.$, (2011) [21], but (i) they are in the Boussinesq domain; and (ii) use an ad-hoc adjustment for the front condition, not a jump relationship. A front condition for the open-top non-Boussinesq gravity current was also suggested by Sciortino et $al.$, (2018) [20]. This result is based on a weak-solution Rankine-Hugoniot derivation, which, in contrast to Benjamin and Ungarish [2], does not satisfy rigorously flow-force equilibrium, energy dissipation validity, and sub-critical speed propagation; and hence it is mostly of academic value. Sciortino et $al.$, (2018) [20] performed accurate experiments for full-depth release currents with open surface in the non-Boussinesq regime $0.6 \leq r \leq 0.86$. They reported reduction of speed of propagation accompanied by a depression of the surface; both effects are more enhanced as r decreases. Unfortunately they did not consider partial-depth release systems, and did not compare with time-dependent solutions of the lock-release problem. To our knowledge, Navier-Stokes simulations for this problem are also unavailable.

In the present paper, we advance existing knowledge on GCs by: (i) developing a new two-layer SW model for the non-Boussinesq case; (ii) solving numerically the resulting lock-release problem; (iii) validating the numerical

results with experiments; (iv) comparing SW and experimental results with a more complex Computational Fluid Dynamics code (CFD).

In particular, we performed a validation of the SW model with the experiments with accurate measurements of the space- and time-varying free surface depression modulated by the advancing current, with the detection of a bounded wave tight to the front and of free waves generated by the impulsive release of the denser fluid in the lock. The detection of the bounded wave is the most striking validation of a two-layer model without lid, with a shape of the trough of the wave computed with the SW model in fairly good agreement with the experimental shape. As a further confirmation of the correctness of the assumptions, we found that in presence of the lid (a classical condition in GCs flow in channels) a bounded wave of the pressure field develops, again with a good agreement between theory of the SW model and experiments (the comparison was made with a conversion of the experimental pressure into hydraulic head). That means that the top boundary condition only affects the manifestation (free surface wave and pressure wave) of an intrinsic characteristic of the flow, well captured by the model. To corroborate and to improve the knowledge of the structure of the flow field, we performed direct measurements of the velocity of the current, also with the aim to present more data for future extended and more comprehensive models. However, we deliberately choose to take the SW model as simple as possible, with assumptions not requiring the experimental estimation of parameters, with rigorous respect of the control-volume balances and of the energy based conditions. More comprehensive models can be developed and implemented in numerical computations (including e.g., entrainment and density variations effects, turbulent structure, friction, coupling between free surface waves and current, secondary circulation in the head of the current), but they all require the introduction of parameters for an appropriate reproduction of the experiments. Unless the numeric value of the parameters is constant in a wide variety of conditions (a quite rare event), the introduction of parameters reduces the generality and the strength of the model. We also remark that the more detailed CFD models are a very time-consuming tool. That renders difficult the calibration of the adjustable parameters and also the simulation of the flow with an adequate combination of the conditions.

The maximum density of the currents in the experiments was limited by some practical aspects, since it is difficult to obtain Newtonian fluid with limited viscosity (high viscosity reduces the Reynolds number of the experiments) and high mass density by adding salts to water. However, the design

of our experiments was dictated by the need of an amplification of the depression of the free surface generated by the advancing current, with a high value of the ambient fluid depth, a relatively long lock (two different values of the lock length were tested for detecting its possible effect on the phenomena under study), and a long channel. The high value of the ambient fluid depth, in addition to an amplification of the depression of the free surface, had other important advantages: (i) the coherent structures travelling toward the free surface and generated by the current advancing in the ambient fluid, hit the free surface and modify its shape [see, e.g., 22, 23], but are smoothed out and diffused during their long travel, with a reduction of their disturbing effects (the mechanism of generation and transport of these coherent structure is detailed in [24] for wall boundary layers); (ii) partial-depth experiments (which are a further validation of the model in a variety of conditions) are possible with a still accurate measurement of the depression of the free surface.

Also the length of the channel was fixed in order to delay the appearance of the free waves reflected by the end wall (the reflected waves are not modelled in the SW model and represent an undesirable interference). The active or passive absorption of the free surface waves is feasible, but in practice, in order to reduce the uncertainties, it is preferable to have a time window during the experiments where the sections of measurements are not yet interested by the reflected waves, and the current advances as if it were in an infinitely long channel.

As last notice, in the experimental conditions characterized by a large depth of the ambient fluid, the experiments were characterized by high Reynolds number with a very limited effect of viscous forces which are neglected in the adopted SW model.

The paper is structured as follows. In §2 the GC conceptual model is detailed, while the finite differences approach adopted and the numerical results obtained are presented in §3 and in §4 respectively. The experimental layout is described in §5, and the experimental results are outlined in §6. Finally, §7 includes the discussion and the conclusions. Appendix A describes the CFD code used for direct simulation of the flow field, and presents detailed results and comparisons for the velocity field and the free surface evolution.

2. SW model

Consider a two-layer system, with densities $\rho_2 < \rho_1$, heights h_1, h_2 and averaged $x-$ velocities u_1, u_2. x is the horizontal coordinate, z the vertical
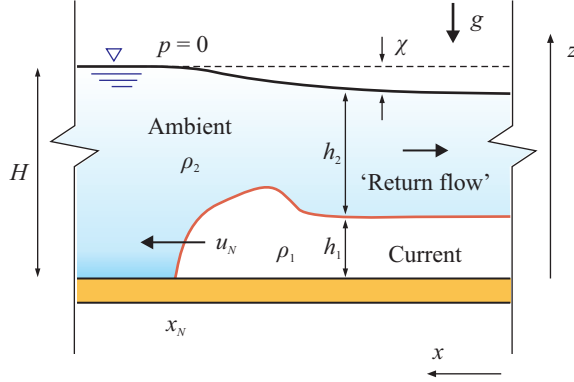
Figure 1: Gravity current with free–surface top open to a constant pressure.

with $z = 0$ at the bottom, the gravity g acts in $-z$ direction, see Figure 1. The height of the undisturbed ambient fluid is H, and initially $h_1 + h_2 = H$, but this does not hold during the motion in the activated domain $x \leq x_N(t)$, where in general results $h_1 + h_2 + \chi = H$. In the covered (fixed top) system, $h_1 + h_2 = H$ is satisfied all the time.

Let $\varepsilon = \rho_1/\rho_2 - 1$, $g' = \epsilon g$. The justifications of the shallow-water approximation for a high-Reynolds-number gravity current have been discussed in the literature [e.g. 3]. The interface between the lower layer 1 and upper layer 2 is assumed sharp, and there is no entrainment/mixing. The current is assumed thin with respect to its length, i.e. $h_0/x_0 \ll 1$, where h_0 is the thickness of the current in the lock and x_0 is the length of the lock, and the equations are formulated in terms of the layer-thicknesses $h_{1,2}$ and $z-$averaged $x-$velocities $u_{1,2}$. In this framework the $z-$ acceleration terms are negligibly small, and hence the pressure is hydrostatic, subject to $p = 0$ at $z = h_1 + h_2$, and thus given by

$$p_2(z) = g\rho_2(h_1 + h_2 - z) \qquad (h_1 \leq z \leq h_1 + h_2), \tag{1}$$

$$p_1(z) = g[\rho_2 h_2 + \rho_1(h_1 - z)] \qquad (0 \leq z \leq h_1), \tag{2}$$

and hence the driving pressure gradients are

$$\frac{\partial p_1}{\partial x} = g\left(\rho_1 \frac{\partial h_1}{\partial x} + \rho_2 \frac{\partial h_2}{\partial x}\right), \quad \frac{\partial p_2}{\partial x} = g\rho_2 \frac{\partial(h_1 + h_2)}{\partial x}. \tag{3}$$

The equations of continuity and the expressions for the $x-$ inertia acceleration terms are like in the covered-channel case (see chapters 2, 3, 5 in Ungarish, 2009 [3]).

6

Scale h_i $(i = 1,\ 2)$ with h_0 in the lock, x with x_0 of the lock, u_i with $U = (\epsilon g h_0)^{1/2}$, t with x_0/U, pressure with $\rho_2 U^2 = \rho_2 g' h_0$. Herein the variables are non dimensional unless differently stated.

The free parameters of the problem are ϵ (or $r = \rho_2/\rho_1 = (1+\epsilon)^{-1}$) and H (height ratio of unperturbed ambient to h_0). The dimensionless equations of motion are

$$(h_i)_t + (h_i u_i)_x = 0 \quad (i = 1, 2), \tag{4}$$

$$\frac{\partial u_1}{\partial t} + u_1 \frac{\partial u_1}{\partial x} = -\frac{1}{\epsilon} \frac{\partial}{\partial x} \left(h_1 + \frac{1}{1+\epsilon} h_2 \right), \tag{5}$$

$$\frac{\partial u_2}{\partial t} + u_2 \frac{\partial u_2}{\partial x} = -\frac{1}{\epsilon} \frac{\partial}{\partial x} (h_1 + h_2). \tag{6}$$

Equations (4)–(6) are a variant of the shallow-water equations developed in [3] chapters 2.1 and 5.2. Here we replace the condition $h_1 + h_2 = H = \text{const.}$ with the condition that the pressure at $z = h_1 + h_2$ is a constant, as detailed in eqs.(1)–(3).

We consider a current of fixed volume released from rest from a lock. The initial and boundary conditions are:

- $h_1 = 1, h_1 + h_2 = H$, $u_1 = u_2 = 0$, for $0 \leq x < 1$ and $t = 0$, $x_N(t = 0) = 1$;

- at $x = 0$, $u_1 = u_2 = 0 \ \forall t$;

- at the nose $x = x_N(t)$, $u_N = u_1 = Fr h_1^{1/2}$, $h_2 = H - h_1 - \chi$ and $u_2 = -u_1(h_1 + \chi)/h_2$, where χ is the depression of the surface at the nose.

Fr and χ are the jump conditions formulated in [2]. For given ϵ and H, they are functions of h_1 only, see § 2.1.

Again, the free parameters of the problem are ϵ and H. The difficulty (and major difference from covered top) is that the pressure terms are now, formally, $O(1/\epsilon)$. This is because the layers of fluid contribute $\rho g h$ pressure terms, while the momentum terms are like $\rho g' h$. This introduces some new time (and speed) scale in the problem, as elaborated in § 2.2. It is convenient to introduce the scaled surface-height variable

$$\phi(x, t) = [(h_1 + h_2) - H]/\epsilon. \tag{7}$$

7

We expect that ϕ is of the order unity for a wide range of ϵ, including the Boussinesq systems with $\epsilon \ll 1$. The boundary (jump) conditions at the nose, discussed below, impose $-\phi(x_N, t) = \chi/\epsilon = h_1(1 - Fr^2/2) < h_1 < 1$, for any ϵ. We argue (and later confirm) that this sets the order of magnitude of $|\phi|$ as $\sim 0.5 h_1 \sim 0.5$ for the whole domain of interest $0 < x < x_N(t)$. Using the ϕ variable, the momentum equations read

$$\frac{\partial u_1}{\partial t} + u_1 \frac{\partial u_1}{\partial x} = -\frac{1}{1 + \epsilon} \frac{\partial}{\partial x} \left(\phi + h_1 \right), \tag{8}$$

$$\frac{\partial u_2}{\partial t} + u_2 \frac{\partial u_2}{\partial x} = -\frac{\partial \phi}{\partial x}. \tag{9}$$

The elimination of ϕ yields

$$\frac{\partial u_1}{\partial t} + u_1 \frac{\partial u_1}{\partial x} - \left[\frac{1}{1 + \epsilon} \left(\frac{\partial u_2}{\partial t} + u_2 \frac{\partial u_2}{\partial x} \right) \right] = -\frac{1}{1 + \epsilon} \frac{\partial h_1}{\partial x}. \tag{10}$$

When $u_2/[(1 + \epsilon)u_1]$ is small, the term in the brackets is negligible, and we obtain the one-layer model equation. We observe that the simplified one-layer model does not preserve the influence of the open surface (expressed by h_2, or ϕ).

2.1. Conditions at the nose

At $x = x_N(t)$ we use the jump conditions derived by Ungarish, (2017) [2] using the control-volume method of Benjamin, and employing two downstream profiles (vortex sheet and vortex wave). The jump satisfies balances of volume, flow-force, pressure-loop and vorticity, and is then subject to physical energy dissipation and sub-critical speed restrictions. We note in passing that a different weak-solution-type front condition has also been suggested by [20], but without performing a flow-force analysis, energy-validity assessment, and criticality consideration, as presented in [2]. We use here the more rigorous results which are easily implemented as follows. The dense current propagates with $u_1 = Fr h_1^{1/2}$, while the total height of the upper surface is reduced from H to $H - \chi$. Let $a = h_1/H, \tilde{\chi} = \chi/H$. For given a and ϵ the values Fr and $\tilde{\chi}$ are provided by the solution of the system

$$\frac{1}{2} Fr^2 \left(\frac{1 + a + \tilde{\chi}}{1 - a - \tilde{\chi}} - \frac{1}{2} \tilde{\chi} \right) = 1 - \frac{1}{2}(a + \tilde{\chi}), \qquad \tilde{\chi} = \epsilon a (1 - \frac{1}{2} Fr^2), \tag{11}$$

constrained by the dissipation condition to $a < 0.5/(1 + \epsilon)$ (approximately, see Ungarish, 2017 [2] for details). The solution is easily obtained by iterations;

8

a convenient starting value is Benjamin's $Fr^2 = (2-a)(1-a)/(1+a)$. A rigorous test for physical dissipation is $Fr/\sqrt{2} \leq 1 - a - \tilde{\chi}$.

2.2. Characteristics and critical conditions

The eigenvalues λ of the system (4)-(6) are given by the equation

$$\epsilon(u_1 - \lambda)^2(u_2 - \lambda)^2 - (u_1 - \lambda)^2 h_2 - (u_2 - \lambda)^2 h_1 + \frac{1}{1+\epsilon}h_1 h_2 = 0. \quad (12)$$

The eigenvalues are in the background of the development and implementation of the SW finite-difference scheme. They indicate a hyperbolic problem and are used to calculate the critical nose restriction reported in the following eq. (18).

2.2.1. The unperturbed fluid domain

Here $u_1 = u_2 = 0$. We obtain the reduction

$$\epsilon\lambda^4 - (h_1 + h_2)\lambda^2 + \frac{1}{1+\epsilon}h_1 h_2 = 0, \quad (13)$$

which yields

$$(\lambda^2)_{1,2} = \frac{1}{2\epsilon}\left\{(h_1 + h_2) \pm \left[(h_1 + h_2)^2 - 4\frac{\epsilon}{1+\epsilon}h_1 h_2\right]^{1/2}\right\}. \quad (14)$$

For small ϵ, by a series expansion, we find four eigenvalues,

$$\lambda_{1,2} \approx \pm\left(\frac{h_1 h_2}{h_1 + h_2}\right)^{1/2}, \quad \lambda_{3,4} \approx \pm\left(\frac{h_1 + h_2}{\epsilon}\right)^{1/2}. \quad (15)$$

We note that for small ϵ (the Boussinesq system) very rapid perturbation waves ($\lambda_{3,4}$) appear in the open-surface configuration, which have no counterpart in the covered system. We recall that the fixed-top system ($h_1 + h_1 = H$) has only two characteristics, which for the unperturbed fluid domain coincide with $\lambda_{1,2}$ for any $\epsilon > 0$.

2.2.2. The critical nose

At the front $x = x_N(t)$ the dense fluid satisfies the jump condition $u_1 = Fr h_1^{1/2}$. The critical situation is when this also satisfies $u_1 = \lambda$. Substitution of these conditions into (12) gives

$$(u_2 - u_1)^2 = \frac{h_2}{1+\epsilon} \quad (x = x_N), \quad (16)$$

9

while the jump condition at the nose imposes

$$u_1 = Fr h_1^{1/2}, \quad u_2 = -u_1 \frac{a + \tilde{\chi}}{1 - a - \tilde{\chi}}, \quad h_2 = H(1 - a - \tilde{\chi}), \qquad (17)$$

where $a = h_1/H$, $\quad \tilde{\chi} = \chi/H$. Combining the equations we obtain the critical nose restriction

$$Fr^2 a \leq \frac{(1 - a - \tilde{\chi})^3}{1 + \epsilon}. \qquad (18)$$

We emphasize that both a and $\tilde{\chi}$ are scaled with the height of the unperturbed ambient H. Thus, in practice, the thickness of the current, h, and of the surface depression, χ, will increase with H (with the input dimensionless parameters ϵ and h_0/H unchanged).

3. Finite difference approach

The SW lock-release problem contains four variables (u_1, u_2, h_1 and h_2 or ϕ) of x and t, with jump conditions at $x_N(t)$ and characteristics given by a 4th-order equation. We could not find analytical solutions and therefore we developed a simple finite-difference solver.

We use the conservation variables h_1, h_2, q_1, q_2, where $q_i = h_i u_i$. A manipulation of (4) and (8)-(9) yields

$$(h_i)_t + (q_i)_x = 0 \quad (i = 1, 2), \qquad (19)$$

$$\frac{\partial q_1}{\partial t} + \frac{\partial}{\partial x}\left(\frac{q_1^2}{h_1} + \frac{1}{1 + \epsilon}\frac{1}{2}h_1^2\right) = -\frac{1}{1 + \epsilon}h_1\frac{\partial \phi}{\partial x}, \qquad (20)$$

$$\frac{\partial q_2}{\partial t} + \frac{\partial}{\partial x}\left(\frac{q_2^2}{h_2}\right) = -h_2\frac{\partial \phi}{\partial x}, \qquad (21)$$

where, again,

$$\phi(x, t) = [(h_1 + h_2) - H]/\epsilon. \qquad (22)$$

The variable ϕ is a robust quantity for a wide range of ϵ. The values of ϵ may be small for the Boussinesq $\rho_2/\rho_1 \approx 1$ case, order of unity when $\rho_2/\rho_1 \approx 0.5$ and large when ρ_2/ρ_1 is small. The variable ϕ is expected to be of the order of unity for these various cases, and hence a convenient variable for the numerical approach to the solution.

We introduce the transformation $y = x/x_N(t)$, see [3] Sect. 2.3, and solve on a fixed grid $y \in [0, 1]$ using fixed δy intervals. We use a MacCormack

10

predictor-corrector scheme [3, App. A2]. To dampen spurious numerical oscillation we added on the rhs of each equation an artificial diffusion/viscosity term of the form $b(\delta x)^2 v_{xx}$, where v is the main variable of the equation and b is of the order of unity ($\delta x = x_N \delta y$). The magnitude of the added term is of the order of magnitude of the truncation error of the scheme, and hence the global consistency and accuracy properties of this well-tested numerical method are maintained. We used typically 200 - 400 space intervals, and the time step δt was set typically to $0.2\delta y$ (the evaluation of the precise CFL condition requires a cumbersome calculation which was not attempted). The numerical accuracy has been tested by running some cases on different grids and with different values of b. The formulation of the code is singular for $H = 1$, and hence we approximate the full-depth release by $H = 1.01$.

4. SW Results

We present solutions for the full-depth release with $r = 0.905, 0.837$ and for $H = 2$, with $r = 0.837$. This corresponds to the laboratory experiments 5, 4, 17, and 10 (Table 1). We also present SW results for the case $H = 1, r = 0.700$ which corresponds to the CFD experiment C16 (Table 1). The results are displayed in Figures 2-6. For $H = 1$ the SW initial propagation is with critical u_N (see (18)). In scaled form, the difference between the $r = 0.905$ and 0.837 cases is very small. However, the change to the partial-depth $H = 2$ produces a significant increase of u_N, and a reduction of the slumping length/time during which u_N is constant.

The depression of the surface is represented by ϕ. We keep in mind that this variable is scaled with ϵh_0, and since $\epsilon = 0.105$ and 0.195 in the cases considered, we conclude that the physical displacement χ of the surface is small. We note that there is a good correlation between ϕ and h_1: the depression is more significant over the domain where the current is thicker. The interpretation is as follows: a larger h_1 causes a larger return flow $|u_2|$ in the ambient, and hence an increase of the kinetic energy for a particle on the streamline. Bernoulli's equation with a constant $p = 0$ on the surface implies that the increase of kinetic energy must be compensated by the decrease of potential energy at the lower position. Therefore, the SW current on the bottom has a clear "fingerprint" on the top surface. This is confirmed by the experiments.

The finite-difference results display some oscillations in places of sharp changes of the variables. This is the manifest of the small numerical dis-
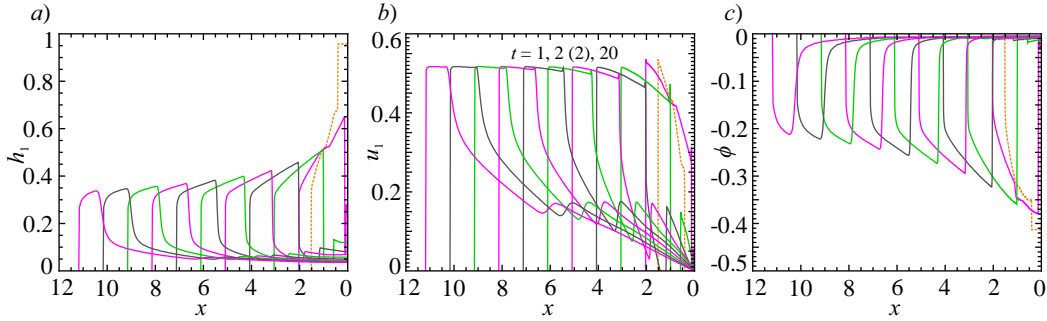
11

Figure 2: SW results, simulation of Expt 5 with $r = 0.9050, H = 1$. *a*) Thickness of the current, *b*) average velocity of the current and *c*) free surface depression at $t = 1, 2, ..., 20$ with a time step equal to 2.

persion of the finite-difference solver, see for example Morton & Mayers [25] Figures 4.7 and 4.12, 4.14. The relevant theory and tests with different grid intervals indicate that the influence of these oscillations on the main solution is negligible. We found that the code is numerically unstable for currents outside the range of validity and criticality of the nose condition. It is not clear what is the physical meaning of this observation. The lock-release currents produced in our experiments were stable; however, the flow adjusted on its own to the nose conditions and hence the energy validity and criticality are intrinsically fulfilled. SW solutions were obtained for other values of H and r, not shown here. The behaviour of the flow field is quite similar to the reported cases. Overall, the SW dam-break with open top problem results are qualitatively and quantitatively quite close to the covered-bottom results. In both cases the initial propagation is with constant u_N (the slumping stage); and change from the full-depth lock $H = 1$ to part depth lock ($H = 2$ say) yields an increase of u_N and decrease of the slumping the length. The major difference observed is the dip of the open-top surface, which provides an upper "fingerprint" of the location of the current. The speed of propagation is slightly smaller in the open-top case, as discussed in more detail in §6.

5. The experimental layout and procedures

To assess the theoretical models, enhancing at the same time the database for this type of flows, a series of specially-designed laboratory experiments was performed at the Hydraulic Laboratory of the University of Parma. A rectangular cross-section channel 30 cm wide and 965 cm long, with glass
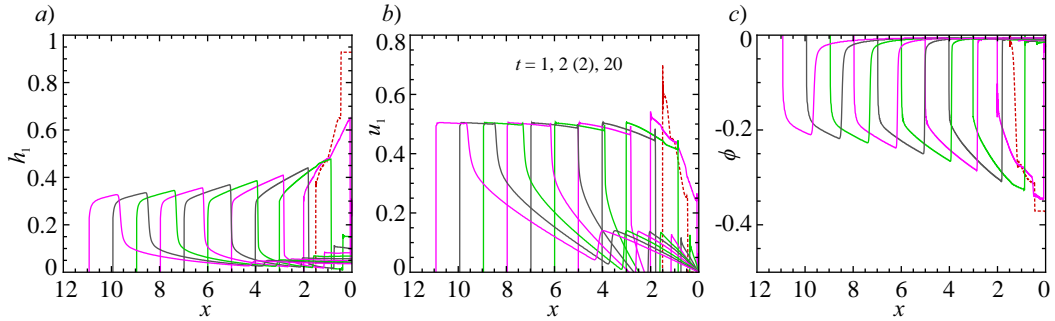
Figure 3: SW results, simulation of Expts. 4-8-17 with $r = 0.837, H = 1$. For caption see Figure 2.
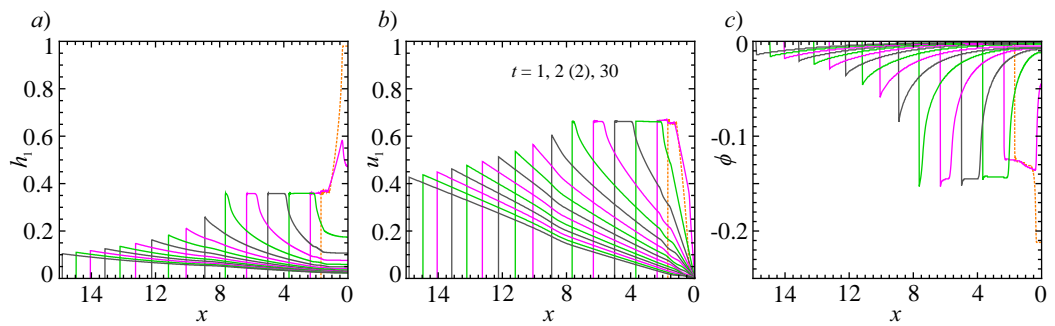

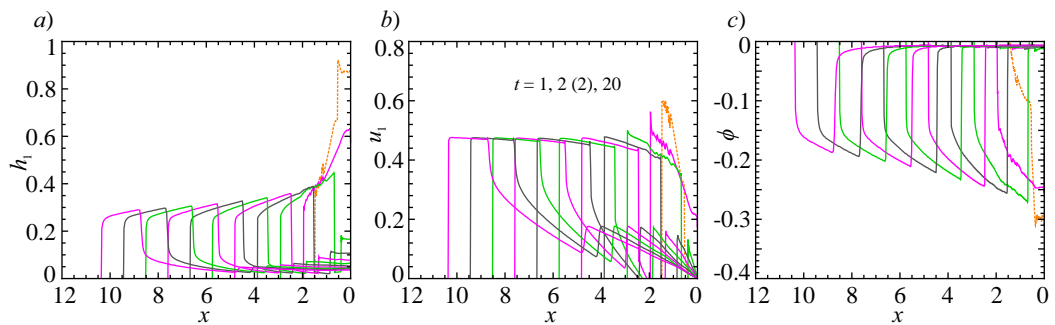Figure 4: SW results, simulation of CFD Expt C16 with $r = 0.700, H = 1$. For caption see Figure 2.

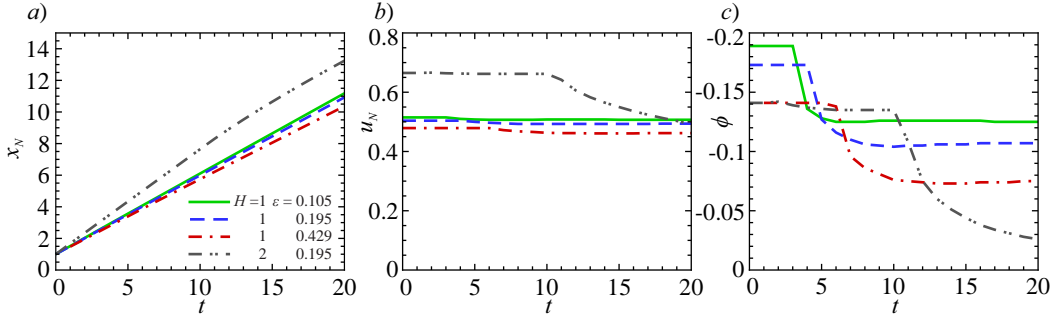Figure 5: SW results, simulation of Expt 10 with $r = 0.837, H = 2$. For caption see Figure 2.

13

Figure 6: SW results for the nose vs t for $H = 1$, $r = 0.905, 0.837, 0.700$ ($\epsilon = 0.105, 0.195, 0.429$), and $H = 2$, $r = 0.837$ ($\epsilon = 0.195$). a) Front position, b) front speed and c) depression in correspondence of the nose of the current.

lateral walls and stainless steel bottom wall was used, with a lock length of $55 - 102$ cm, see Figure 7ab. The gate was a stainless steel plate, 0.2 cm thick, rapidly lifted with a cable and pulleys system. The opening of the gate took approximately 0.2 s.

In a first series of tests the ambient fluid, tap water of density equal to $\rho_2 = 0.998$ g cm^{-3}, had a free surface. The intruding current was prepared in an ad-hoc tank by adding sodium chloride (NaCl) to tap water and introducing aniline dye into the latter for an easy visualization of the shape of the current advancing in the transparent ambient fluid. The use of NaCl allowed the intruding current to reach a maximum final density of $\rho_1 = 1.193$ g cm^{-3} ($r = 0.836, \epsilon = 0.195$). Several marks with a 20 cm spacing where stuck on the bottom in order to measure the front speed; a grid with 5 cm horizontally spaced and 1 cm vertically spaced lines was stuck on the side of the channel in order to measure the amplitude of the oscillations of the free surface by converting the pixel position of video images into metric coordinates. The procedure of filling the tank was designed in order to avoid excessive net force on the gate. Initially the downstream channel was filled with tap water up to a target level corresponding to the zero level of the grid. Then the high density fluid was gently poured inside the lock. In order to reduce the hydraulic disturbances due to the lift of the gate, two horizontal polystyrene lids were fixed on both sides of the gate and maintained in contact with the surface of both the ambient and the intruding fluids. In this way, the oscillations of the free surface triggered by the vertical movement of the gate were minimized.
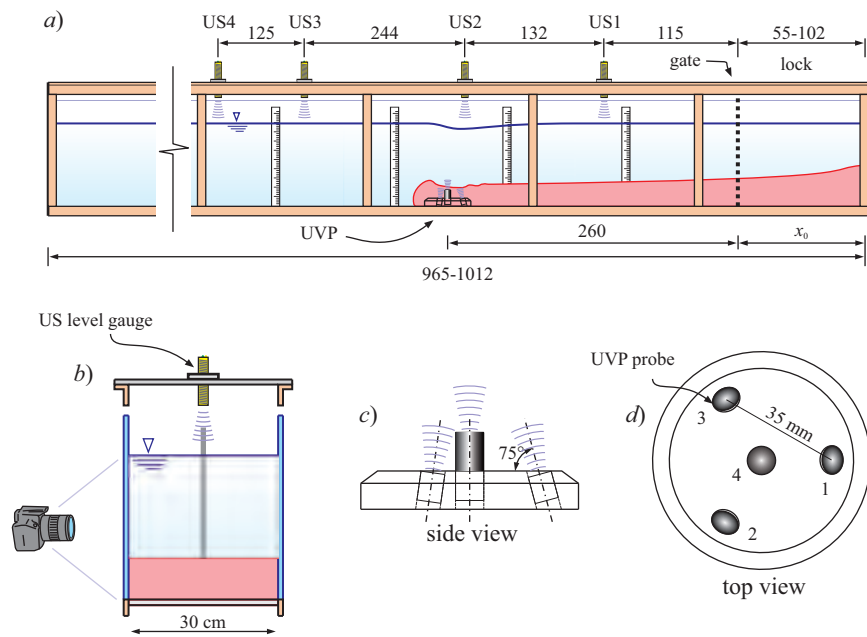
14

Figure 7: Layout of the experimental set-up. *a*) The channel with the four Ultrasound distance meters and the section of measurements of velocity trough the UVP; *b*) cross section of the channel; *c*) side view and *d*) top view of the arrangement of the four UVP probes. Distances are in centimetres.

15

Each experiment was recorded by three high-resolution video-cameras (3840×2160 pixels) working at 30 frames per second (f.p.s.), each of them with a Field of View (FOV) ≈ 1 m long in the horizontal direction. High-frequency neon lights were adopted as a uniform and stable source of illumination from the side of the channel. After extraction of the frames from the videos using a commercial software, it was possible to detect the profile of the free surface using a proprietary software with a time accuracy of $1/30$ s. In order to trigger the start of the flow, the opening of the gate was detected by a micro-switch which turned off several LEDs when the gate was lifted. The LEDs were positioned along the channel in order to be in the FOV of the video-cameras and to allow synchronizing the frames of the videos.

Three Ultrasound distance meters (US1, US2, US3) (TurckBanner Q45UR) were positioned on the top of the channel to record the free surface oscillations with an accuracy of 0.03 cm and a data rate of 100 Hz. The overall accuracy of measurements of the depression was checked for a single test by comparing the results of the Ultrasound distance meters and of the image analysis. Figure 8 shows the comparison between the free surface elevation χ measured with both techniques at the cross sections of coordinates $x = 115 - 247$ cm (measured from the gate). The agreement is fairly good, considering that no calibration parameters are needed; the small discrepancies between measurements are due to meniscus, which also acts as a filter of the high frequency fluctuations.

Fluid velocity was measured in the mid-section of the channel by an array of four Ultrasound Velocity Profilers (UVP, model DOP 2000 Signal-Processing S.A., Switzerland, 2005) with a carrier at 8 MHz (TR0805LS) and installed at $x = 260$ cm from the gate. The four probes were arranged as in Figure 7cd and in the adopted configuration acquired the three-component velocity profiles in the vertical with a space resolution of 0.11 cm, 120 volumes of measurements and data rate ≈ 18 Hz (number of profiles per second). The raw data are represented by the axial velocity components for probes 1,2 and 3, acquired with a small time lag and then transformed into the Cartesian coordinate system $x - y - z$ with a transformation:

$$\begin{Bmatrix} u \\ v \\ w \end{Bmatrix} = \mathbf{A} \cdot \begin{Bmatrix} u_1 \\ u_2 \\ u_3 \end{Bmatrix}, \tag{23}$$

where $\mathbf{A}$ is the matrix of transformation and u_1, u_2, u_3 are the axial velocities acquired by the three probes. A correction for the time lag is introduced by
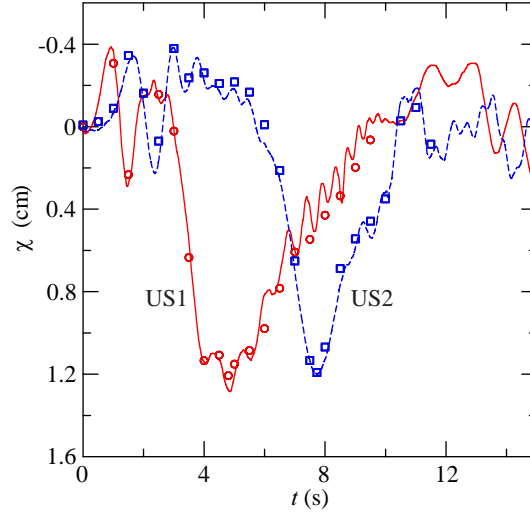
16

Figure 8: Free surface levels measured by two Ultrasound distance meters (continuous and dashed lines) and computed with the image analysis (symbols).

expanding in series, obtaining

$$
\begin{Bmatrix} u(t) \\ v(t) \\ w(t) \end{Bmatrix} = \mathbf{A} \cdot \begin{Bmatrix} u_2(t - \Delta t) \\ u_3(t) \\ u_4(t + \Delta t) \end{Bmatrix} + \mathbf{B} \cdot \frac{\partial}{\partial t} \begin{Bmatrix} u_2(t - \Delta t) \\ u_3(t) \\ u_4(t + \Delta t) \end{Bmatrix} \Delta t + O(\Delta t^2), \quad (24)
$$

and

$$
\mathbf{B} = \begin{bmatrix} A_{11} & 0 & -A_{13} \\ A_{21} & 0 & -A_{23} \\ A_{31} & 0 & -A_{31} \end{bmatrix}. \quad (25)
$$

More details on data analysis from UVP are given in [23]. The central probe (No 4) was used to record the echo in an attempt to detect the current-ambient fluid interface, since the echo of the Ultrasounds is stronger where a variation of acoustic impedance occurs, like at the interface. Figure 9 shows the measured velocity components for Expt 7. The validity of the assumptions used to transform the axial velocities into velocity components along the $x - y - z$ axes can be appreciated by observing the good agreement between the vertical velocity, w, as reconstructed with eq. (24) applied to measurements by probes No. 1-2-3 (symbols) and as measured by probe No. 4 (continuous line). The figure also shows the energy of the echo of probe No 4, with a maximum at a level that can be assumed as representative of the thickness of the current.
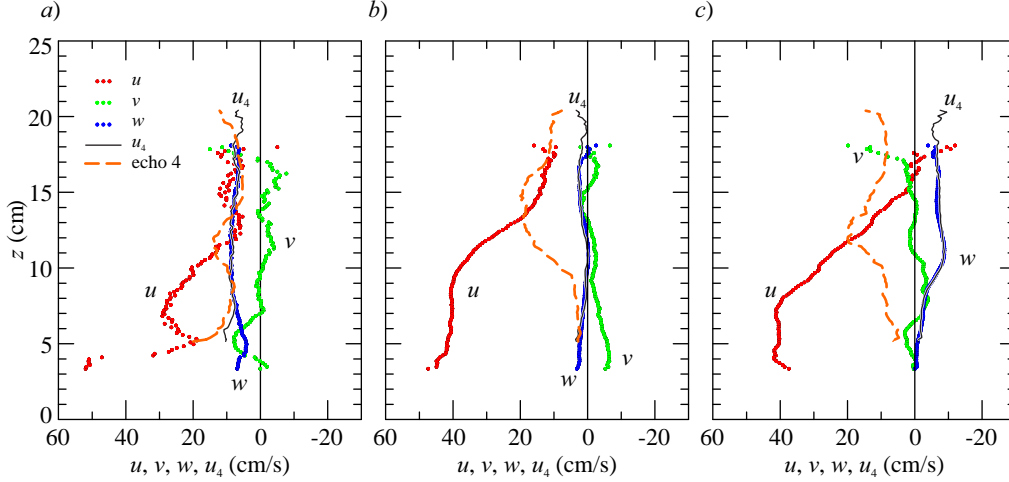
17

Figure 9: Velocity profiles and echo measured for Expt 7. *a*) $t = 7.6$ s; *b*) $t = 8.2$ s; *c*) $t = 8.8$ s. The symbols are the velocity components in the stream wise (u), span wise (v) and vertical (w) directions, the continuous curve almost overlapping with the vertical velocity is the axial velocity of the vertical central probe No 4 (u_4), the dashed curve is the energy of the echo of probe No 4.

The position of the front of the current was detected using a full HD video camera (Canon Legria HF 20, 1920 × 1080 pixels) with data rate of 25 frames per second. The camera was translated parallel to the channel in order to keep the nose of the current in the FOV and the marks stuck at the bottom of the channel were used to detect the front position of the current with an overall uncertainty of less than 0.2 cm.

A second series of experiments were performed with a lid on the top, in order to compare its effects on the front speed of the current. A differential manometer with an overall accuracy of 0.1 mbar was positioned at a distance of 160 cm from the gate, with one port at atmospheric pressure and the second port near the lid and in contact with the ambient fluid, with the aim of measuring the pressure variations due to the advancing current.

5.1. The uncertainty in variables and parameters

The parameters of the experiments are either directly measured or computed on the basis of the measurements. Mass density was measured by a densimeter with an accuracy of 10^{-3} g cm^{-3}, and the corresponding uncertainty for $r = \rho_2/\rho_1$ is $\Delta r/r \leq 0.2\%$. The relative uncertainty in the reduced gravity g' is again 0.2%. The level of the ambient fluid and of

the intruding fluid in the lock was fixed with an accuracy of 0.1 cm and the relative uncertainty is $\Delta H/H \leq 0.3\%$ and $\Delta h_0/h_0 \leq 0.3\%$. The uncertainty on the ratio H/h_0 is at most equal to 0.6%. The velocity scale had an uncertainty $\Delta U/U \leq 0.4\%$ and the time scale had an uncertainty equal to $\Delta T/T \leq 1.4\%$. By assuming an uncertainty of 1% in the value of the kinematic viscosity of the denser fluid, the resulting uncertainty in Reynolds number was $\Delta Re_0/Re_0 \leq 2.0\%$. The free surface level of the ambient fluid measured by the Ultrasonic distance meters had an uncertainty of 0.03 cm. The velocity field reconstructed by using measurements by the UVP probes had an uncertainty of 4% of the measured value, with a minimum of $0.3~\mathrm{cm\,s}^{-1}$. The uncertainty of the vertical position where the velocity measurements are referred was 0.1 cm.

6. The experiments

Eighteen experiments were performed, fourteen with an open boundary and four with a top lid. Table 1 lists the main parameters for each experiment. Note that two additional lines include relevant data for numerical experiments conducted for a system without lid; details about these computer simulations are provided in Appendix A. The purpose of the computer experiments is to simulate markedly non-Boussinesq currents with $r = 0.7$, thus widening the range of parameters under consideration.

To illustrate the general behaviour of the experiments, a sequence of frames is shown in Figure 10 for Expt 17; an enlargement near the free surface is also shown for a better visualization of the free surface distortion due to the advancing GC. It is seen that the free surface is elevated downstream the nose and is depressed behind the nose, with a space lag almost equal to the distance between the front and the first billow.

Figure 11 shows the dimensionless front position of the intruding current for all the experiments. For an easy visualization the symbols related to experiments in partial-depth have been translated of five ($H = 4/3$) and ten units ($H = 2$) in the vertical, respectively, and have been decimated. The data collapse fairly well for each series of experiments; it is seen that the initial slumping phase with a constant front speed is followed by a deceleration which is more evident in partial-depth conditions. There is no significant detectable effect of the free surface waves or of the lock-length on the front speed. However, a small reduction of the slumping phase front speed is detected by comparing, e.g., Expt 7 (open top) and Expt 9 (top-lid),

two experiments with identical parameters but with a different top boundary condition. The open top b.c. allows the development of free surface waves, which subtract part of the potential energy available to accelerate the current. As a result, a reduction of the front speed $\leq 3\%$ is recorded (see Appendix A for details on the energy balance). Similar results are obtained by pairwise comparison of Expts. 11-12, 10-13, 8-4, where Expts.11-10-4 are with a top lid and Expts. 12-13-4 are their open-top counterparts.

Figure 12 shows the dimensionless depression of the free surface profiles for Expt 4 with lock-length $x_0 = 55$ cm. Two families of free surface oscillations can be observed, (i) propagating waves and (ii) bounded waves. In addition to these waves, there are secondary small oscillations coupled to the billows of the intruding current. The front of the current is forerun by a solitary wave propagating with height ≈ 1.5 cm and a celerity equal to ≈ 160 cm/s, and is followed by a trough (bounded wave) with a maximum depression at ≈ 30 cm behind the nose. The solitary wave is similar to the wave generated by an avalanche reaching the sea and generating a tsunami. The maximum trough amplitude is equal to ≈ 2 cm and progressively decreases with the front advancement. After a few seconds, the initial solitary wave is reflected by the end wall and reaches, with negative celerity, the front of the current, partially canceling the trough. Figure 12 also shows: i) the results of the SW numerical code for Expt 4, and ii) the profiles measured for Expt 17, with the same parameters of Expt 4 except for a lock length $x_0 = 102$ cm, i.e. almost double that of Expt 4. Upon comparing the different curves, it is observed that the experimental length of the trough is finite and fairly well predicted by the theoretical model. Moreover, a longer lock generates a more persistent depression of the free surface: the trough length appreciably scales with the length of the lock. In both experiments, the limited length of the trough is a consequence of the limited volume of the lock, which generates a current of finite length instead of a long tongue.

Figure 13a shows a more comprehensive comparison, conducted for all tests, between the depression χ deriving from the experiments and from SW theory. The experimental values (empty symbols) are generally close to the theory (solid lines) with relatively minor deviations. The CFD simulations (filled symbols), conducted for the full-depth case with the free-surface boundary condition (see Appendix A) generally overestimate the SW theoretical values. Depressions resulting from the top-lid boundary condition are also plotted for comparison (crossed symbols) and show deviations both in excess and in defect from the theoretical predictions.

Figure 13b shows the comparison among the four earlier categories of results (experimental open-top, SW theoretical open-top, experimental top-lid, and CFD open-top) for the height h_N at the front of the current. There are discrepancies with the SW theory, especially for the partial depth case, but in general the trend is correctly reproduced, with larger thickness of the current at the nose for partial depth than for full depth experiments. The long error bars associated with experimental results indicate that h_N is subject to a relevant uncertainty which is a consequence also of the difficult definition of the experimental height of the current near the front.

A final comparison is conducted in terms of the front velocity u_N and is shown in Figure 13c. Theoretical SW results always overestimate their experimental counterparts albeit to a variable degree, but almost always larger than the error bars; the agreement is proportionally worse for the full-depth case. The overestimation is a standard result due to the approximations embedded in the SW model, which neglects entrainment and dissipation and adopts the thin layer approximation. The experimental data for $H = 1$ from [20] are also shown, with a good overlap with the present experiments and a good agreement with theoretical predictions.

6.1. The structure of the velocity field

The structure of the velocity fields in GCs has a main role in addressing the complex interaction between the nose, the billows and the ambient fluid, and whenever a more detailed analysis is requested. The SW equations rely on a uniform velocity along the vertical, while other models assume velocity profiles with a prescribed shape in the ambient fluid; an in-depth experimental analysis is requested to clarify the correctness of these assumptions. Past measurements of velocity profiles in GCs with UVP are detailed in [19] where a single probe/two probes was/were used to measure the velocity structure within the ambient fluid. The present measurements are obtained with four probes located within the intruding current. Since the position of the volume of measurements ("gates") and of the Doppler shift require the value of the sound celerity, ($c = \sqrt{\epsilon/\rho}$ where ϵ is the adiabatic bulk modulus), we assumed a constant celerity in the current computed by adopting the theoretical values of the bulk modulus and the mass density of the fluid.

Figure 14ab shows the velocity field measured by the UVP probes for two experiments (Expt 4 and Expt 17) having identical parameters but with lock-length $55 - 102$ cm, respectively. The time series of the velocity measured in a single section has been mapped into space by multiplying the time and the

Expt	H	x_0 (cm)	r	ε	g' ($\mathrm{cm\,s^{-2}}$)	U ($\mathrm{cm\,s^{-1}}$)	T (s)	Re_0 ($\times 10^3$)	
5	1	55	0.905	0.105	103.2	64.2	0.856	214	
6	1	55	0.850	0.176	172.9	83.2	0.661	277	
4	1	55	0.837	0.195	191.6	87.5	0.628	292	
17	1	102	0.837	0.195	191.6	87.5	1.165	292	
14	4/3	55	0.837	0.195	191.6	75.8	0.725	190	
13	2	55	0.839	0.192	188.7	61.4	0.895	102	
19	2	102	0.837	0.194	190.6	61.7	1.652	103	
7	1	55	0.868	0.152	149.3	77.3	0.712	258	
18	1	102	0.867	0.153	150.3	77.5	1.315	258	
15	4/3	55	0.867	0.153	150.3	67.2	0.819	168	
12	2	55	0.868	0.152	149.3	54.7	1.006	91	
20	2	102	0.867	0.153	150.3	54.8	1.860	91	
C16	1	55	0.700	0.429	420.5	129.7	0.424	432	CFD
C16bis	1	102	0.700	0.429	420.5	129.7	0.786	432	CFD
8	1	55	0.839	0.192	188.7	86.9	0.633	290	lid
10	2	55	0.837	0.194	190.6	61.7	0.891	103	lid
9	1	55	0.868	0.152	149.3	77.3	0.712	258	lid
11	2	55	0.868	0.152	149.3	54.7	1.006	91	lid
21	1	102	0.948	0.055	54.0	46.5	2.194	155	
22	4/3	102	0.950	0.052	51.1	39.2	2.605	98	

Table 1: Parameters of the experiments in a rectangular cross-section channel $b = 30$ cm width, filled of ambient fluid with $H = 40$ cm. The last column indicates if an open-top boundary (lid) is present and if the experiment is a CFD numerical simulation.
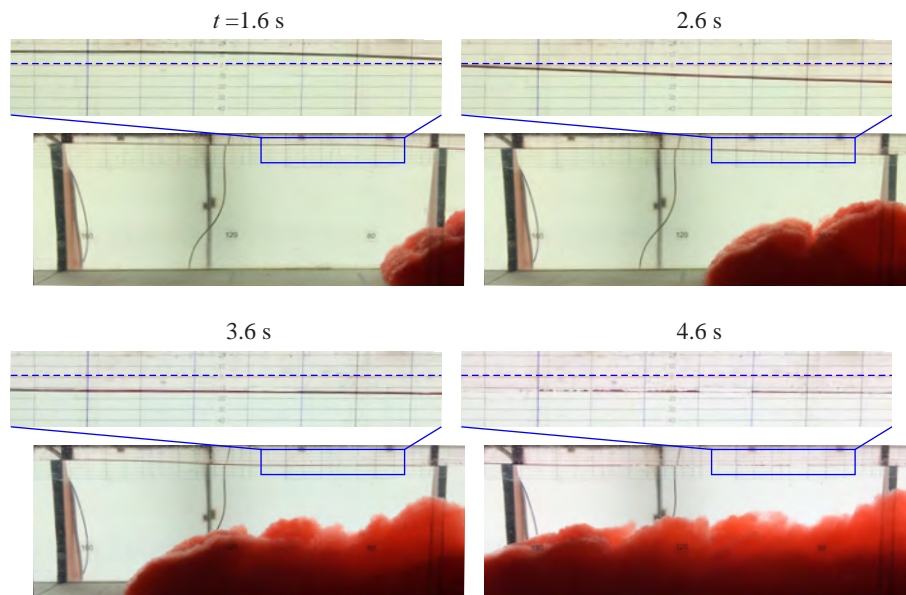
Figure 10: A sequence of frames for Expt 17, full-depth lock release with $r = 0.837$ and $x_0 = 102$ cm. The enlargements show the free surface with a grid step of 10 mm in the vertical and 50 mm in the horizontal direction, respectively. The dashed horizontal line is the still ambient fluid level.
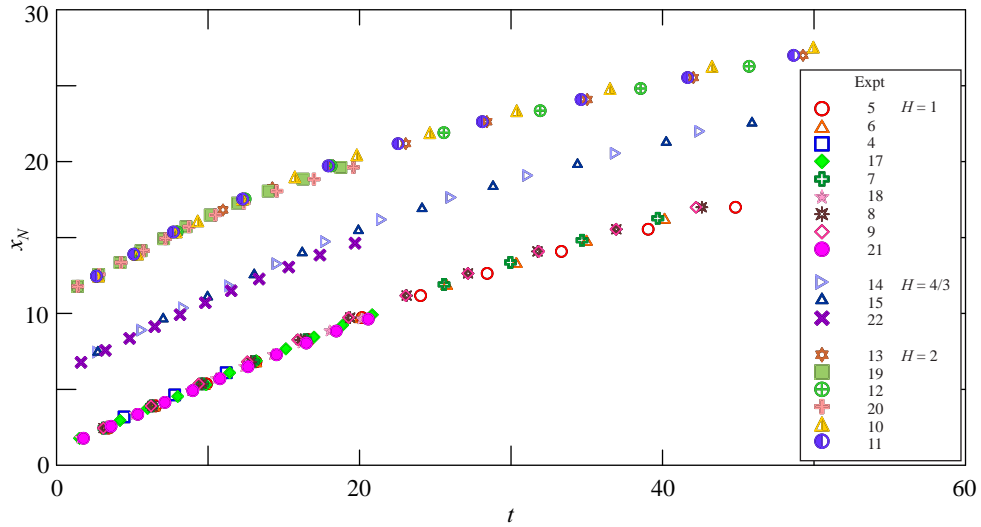
Figure 11: The distance of propagation of the currents measured from the back-wall in the lock for experiments with $H = 1, 4/3, 2$. Empty and filled symbols refer to $x_0 = 55$ cm and to $x_0 = 102$ cm, respectively. One point in two is shown and data for experiments in partial-depth have been translated in the vertical of 5 ($H = 4/3$) and 10 units ($H = 2$) for an easy visualization.

front speed under the hypothesis of "frozen" current: time is mapped into space as $x \rightarrow \dot{x}_n t$. The front speed is almost identical for the two experiments, but the shape of the current is quite different, with a detached body of dense fluid advancing with a limited tail in the experiment with short lock, and a long thin current in the experiment with a long lock.
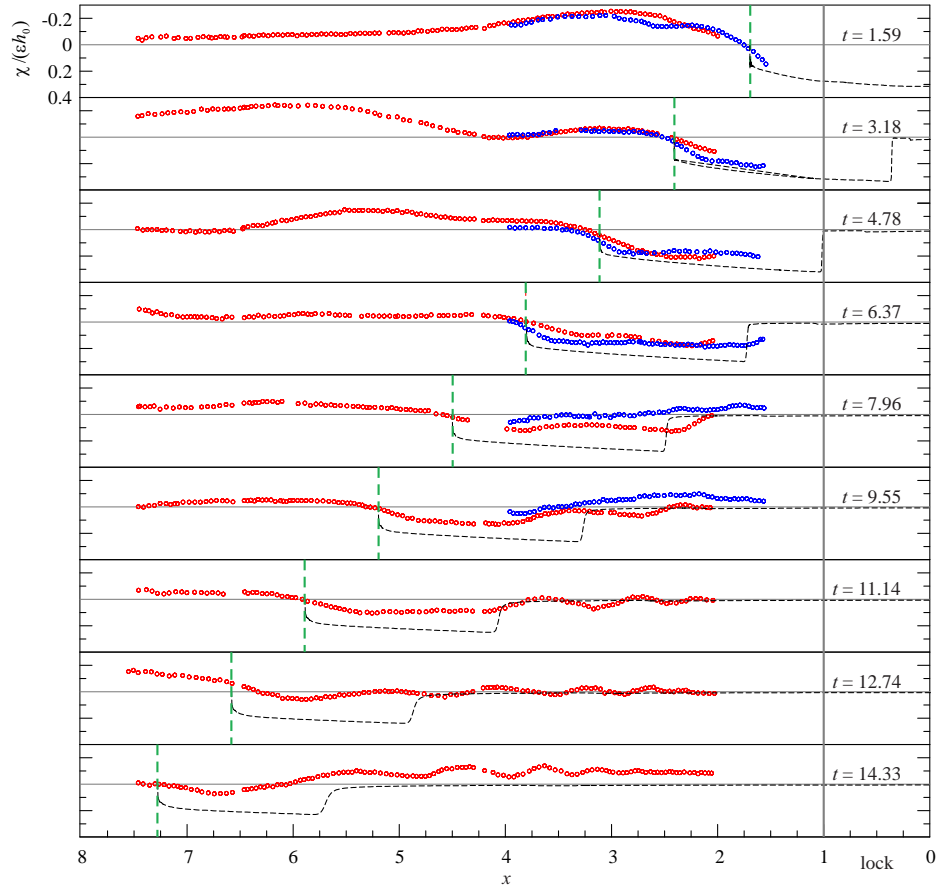
Figure 12: Free surface profiles for Expt 4 with $x_0 = 55$ cm (red symbols) and for Expt 17 (blue symbols), having identical parameters of Expt 4 but with a lock length $x_0 = 102$ cm.The dashed vertical line indicates the front position, the dashed lines are SW numerical model results.
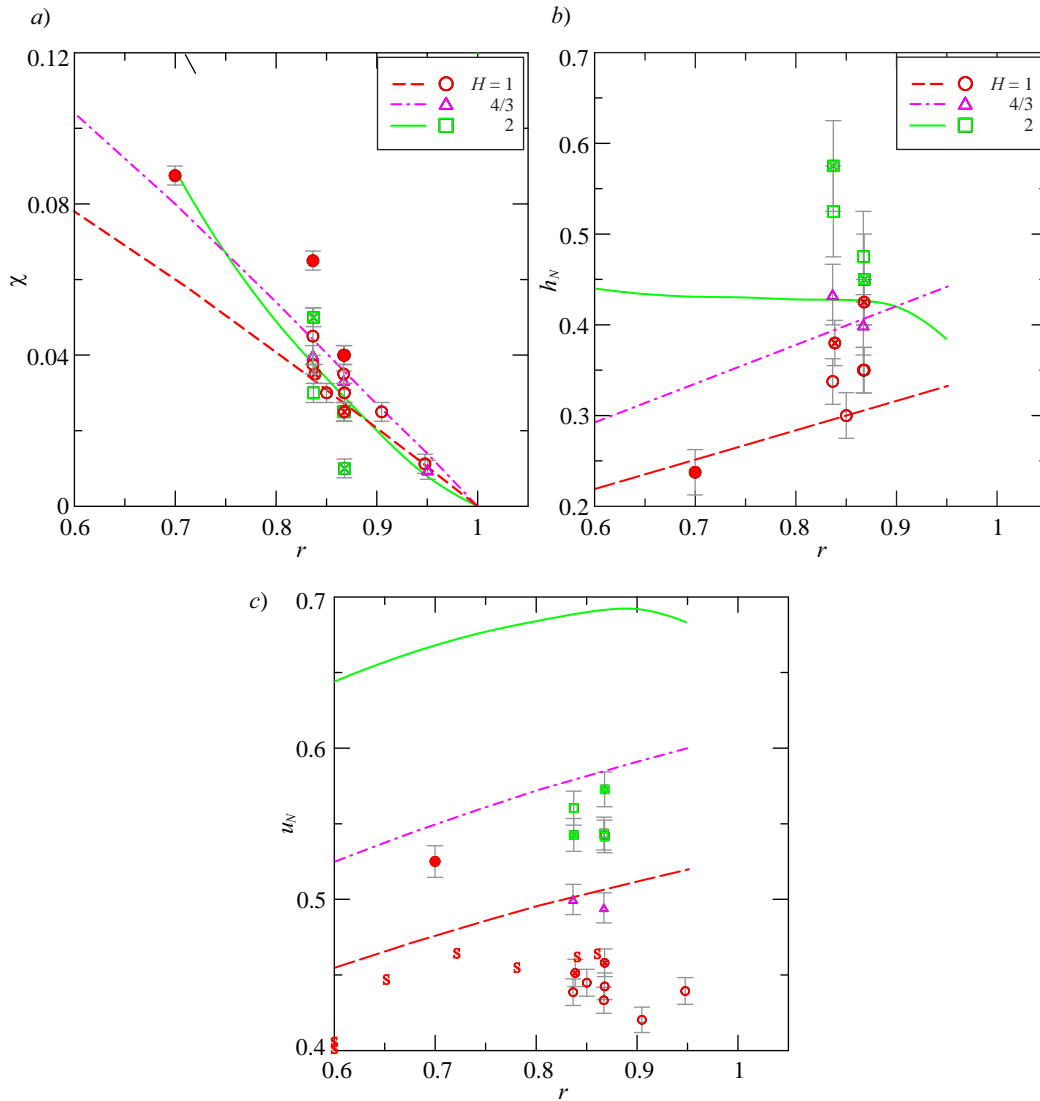
25

Figure 13: Comparison between experiments and theory. a) Depression, b) height of the current at the front, c) front speed. The empty symbols refer to experiments, the curves refer to SW theory, the crossed symbols refer to experiments with a lid, where the virtual depression χ is computed by using a pressure measurement at the top of the channel, the filled symbols refer to the CFD simulation results, the symbols 'S' refer to the experiments in Sciortino et $al.$ (2018) [20] for $H = 1$.
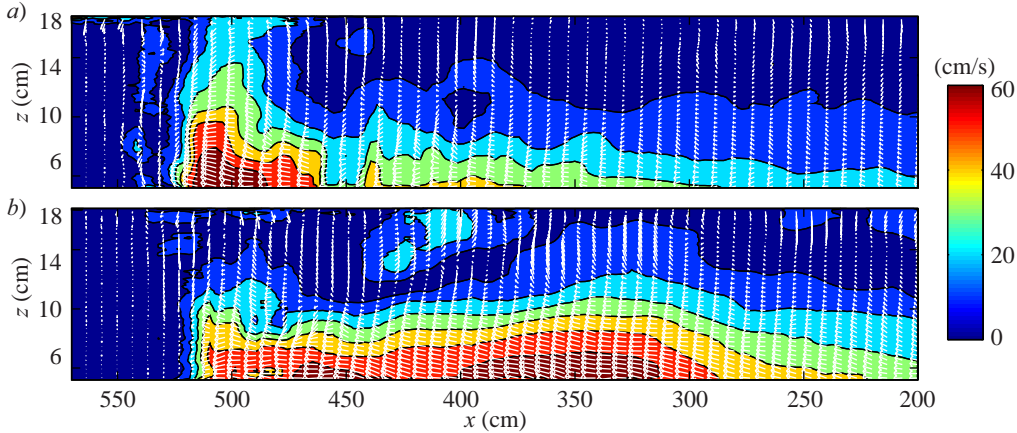
Figure 14: Velocity field reconstructed by using the UVP signal. a) Expt 4, full-depth release, $r = 0.837$, $x_0 = 55$ cm; b) Expt 17, parameters equal to Expt 4 but $x_0 = 102$ cm. The colormap refers to the modulus of the fluid velocity, $\sqrt{u^2 + w^2}$.

7. Discussion and conclusions

Motivated by the ubiquitous presence of gravity currents (GCs) with open-top (free surface) in environmental and industrial applications, we studied the non-Boussinesq regime of inertial GCs performing a series of free-surface experiments in a rectangular cross-section channel, and developing a novel two-layer SW model to interpret the experimental results. The experiments were performed with different values of the density ratio r ranging from 0.950 to 0.837; measured quantities included the free surface depression of the ambient fluid, the thickness and the front speed of the intruding current, and the three components of the velocity by means of a UVP. To extend the study to lower values of r (a difficult task since non dangerous salts to be added to water to obtain heavy fluids with Newtonian rheology are rare and expensive), numerical simulations were conducted with $r = 0.7$ using a numerical commercial CFD code based on RANS. We performed experiments for both full-depth and partial-depth locks. Further, some experiments were repeated with a top-lid, in order to compare the effect of the boundary condition on the front speed and to measure the pressure variation, a proxy for the free surface fluctuations. We think that our work provides useful insights and modelling suggestions concerning the flow of a GC in a system with a free surface.

Our work leads to the following major conclusions:

27

- The high density current advancing in the fluid generates two main families of waves, progressive waves faster than the front, and a trough bounded to the front and lagging it. In a finite length channel the reflection on the back- and end-walls generates further waves which modify in a complex manner the free surface elevation. A depression of the open-top surface is observed in all cases (similar results of [20]) and providing an indication of the location of the front of the intruding current. Specifically, the amplitude of the trough (maximum depression) behind the nose was chosen to compare results from the numerical SW code and the experiments. The experimental amplitude of the trough generally is less than the theoretical one, while the numerical simulations overestimate experimental results.

- The front position of the intruding current collapses on theoretical predictions fairly well, showing that an initial slumping phase with a constant front speed is followed by a deceleration, which is more evident in partial-depth conditions. The prediction of the thickness of the current is subject to a large uncertainty and less good than for the front position, but shows the correct trend for increasing r. As for the front velocity, theoretical results overestimate their experimental counterparts, due to the approximations embedded in the SW model, which neglects entrainment and dissipation and adopts the thin layer approximation. The incorporation of entrainment and bottom friction in SW-type models is formally possible [21], but in this case the solution is reliant on empirical coefficients which, in general, are now known for non-Boussinesq currents. Such an extension requires a dedicated investigation which must be left for the future. We reiterate that the advantage of the SW model used in the present investigation is that it is self contained: the solution is determined by the initial conditions, geometry of the lock, and the density ratio r without any adjustable constant.

- Results for experiments conducted with a covered-bottom are qualitatively and quantitatively quite close to those obtained with the free-surface condition, except for the depression in the ambient induced in the latter case, which also exhibits a slightly smaller speed of propagation. A good comparison between theory and experiments is also obtained for the covered-bottom case; here, the differential pressure

28

variation measured at the top of the channel agrees with the theory and is also well reproduced by the CFD code.

- As to the effect of the lock–length on the overall geometry of the current and of the depression, it is seen that the lock–length does not affect the front speed during the slumping phase, but has an evident effect on the geometry of the current behind the nose and on the length of the depression: the longer the lock, the longer the depression; the shorter the lock, the more similar to a single hump is the current. The length of the through appreciably scales with the lock-length and is generally well reproduced by the SW model.

- The time series of the fluid velocity with the UVP (time series in a single section of the channel) can be transformed into space series by assuming a "frozen" current behaviour and mapping $t \rightarrow \dot{x}_N x$. The correctness of this approach, at least during the slumping phase, has been validated with the CFD code results.

Acknowledgements

Supplementary material

A video of the CFD simulation for Expt C16bis is supplemented, showing the flow field and the advancing density current.

Appendices

A. Volume of Fluid (VoF) numerical model

Since the maximum density of the current fluid obtained adding NaCl is $\rho_1 \lesssim 1.200 \text{ g cm}^{-3}$ a commercial numerical model was adopted to simulate high density GCs. Its calibration was performed by tuning the parameters C_μ in the turbulence model in order to obtain a GC front speed matching the experimental one. C_μ appears in the equation used to compute the turbulent viscosity, μ_t. The propagation of a gravity current in an homogeneous ambient with free surface can be modelled assuming three immiscible phases: (i) the primary ambient fluid (air), (ii) the secondary ambient fluid (fresh water) and (iii) the intruding fluid (brine). An Eulerian numerical model has been implemented using ANSYS Fluent [26], which solves the Reynolds Averaged Navier-Stokes equations (RANS) using the Volume of Fluid (VoF) approach in order to track and locate the free surface (or fluid-fluid interface). The continuity equation can be written as follows:

$$\frac{\partial \rho}{\partial t} + \nabla \cdot (\rho \mathbf{v}) = S_m, \qquad (A.1)$$

where ρ is the fluid density, $\mathbf{v}$ is the velocity vector and t is the time. S_m is a source term, which takes into account the mass added to the continuous phase from the dispersed second phase (e.g., due to vaporization of liquid droplets). Equation (A.1) is valid for incompressible as well as compressible flows.

The momentum balance equation is:

$$\frac{\partial}{\partial t}(\rho \mathbf{v}) + \nabla \cdot (\rho \mathbf{v} \mathbf{v}) = \nabla \cdot p + \nabla \cdot \bar{\tau} + \rho \mathbf{g} + \mathbf{F} \qquad (A.2)$$

where p is the static pressure and $\rho \mathbf{g}$ and $\mathbf{F}$ are the gravitational and the external body forces (e.g. arising from the interaction with the dispersed phase) respectively. $\bar{\tau}$ is the stress tensor, given by

$$\bar{\tau} = \mu \left[\left(\nabla \cdot \mathbf{v} + (\nabla \cdot \mathbf{v})^T \right) - \frac{2}{3} (\nabla \cdot \mathbf{v}) I \right], \qquad (A.3)$$

where μ is the dynamic viscosity and I is the unit tensor.

In a VoF formulation two or more not-interpenetrating fluids (or phases) are present; for each additional phase, a new variable is introduced, i.e. the volume fraction of the phase in the computational cell.

The tracking of the interface(s) between the phases is accomplished by the solution of an additional continuity equation related to one (or more) of the phases. For the i-th phase this equation has the following form:

$$\frac{1}{\rho_i} \left[\frac{\partial}{\partial t} \left(\alpha_i \rho_i \right) + \nabla \cdot \left(\alpha_i \rho_i \mathbf{v} \right) = \sum_{j=1}^{n} \left(\dot{m}_{ji} - \dot{m}_{ij} \right) \right], \qquad (A.4)$$

where α_i is the volume fraction $(0 \leq \alpha_i \leq 1)$ of the $i - th$ phase, $\dot{m}_{ij}$ is the mass transfer from phase i to phase j and $\dot{m}_{ji}$ is the mass transfer from phase j to phase i.

The implicit scheme was used for time discretization and the "Implicit Body Force" treatment for the Body Force Formulation in the Multiphase Model was enabled. This treatment improves the convergence of solutions by accounting for the partial equilibrium of the pressure gradient and body forces in the momentum equations. The Reynolds Stress Model (RSM) was adopted. Abandoning the isotropic eddy-viscosity hypothesis, the RSM closes the Reynolds-averaged Navier-Stokes equations by solving transport equations for the Reynolds stresses (which appear in equation (A.2) when the Reynolds decomposition is applied), together with an equation for the dissipation rate. A series of numerical tests demonstrated that the RSM it the turbulence model that provide the best agreement between the results from FLUENT simulation and the experimental data from [27]. Both the options "Wall BC from k equation" and "Wall Reflection Effects" were enabled, respectively (i) to allow the explicit setting of boundary conditions for the Reynolds stress model near the walls and (ii) to calculate the component of the pressure strain term responsible for the redistribution of normal stresses near the wall.

The Pressure-Implicit with Splitting of Operators (PISO) scheme was adopted for the pressure-velocity coupling, and a second order discretization scheme was used for both momentum and volume fraction. In this method, under-relaxation factors greater than 0.8 are recommended for all equations, except for for momentum and pressure factor that were set respectively equal to 0.7 and 0.3 (default values). Also a volume fraction factor equal to 0.5 can be adopted. At the beginning of the simulation a time step equal to 0.0001 s was set in order to get a stable solution; then the time step was gradually
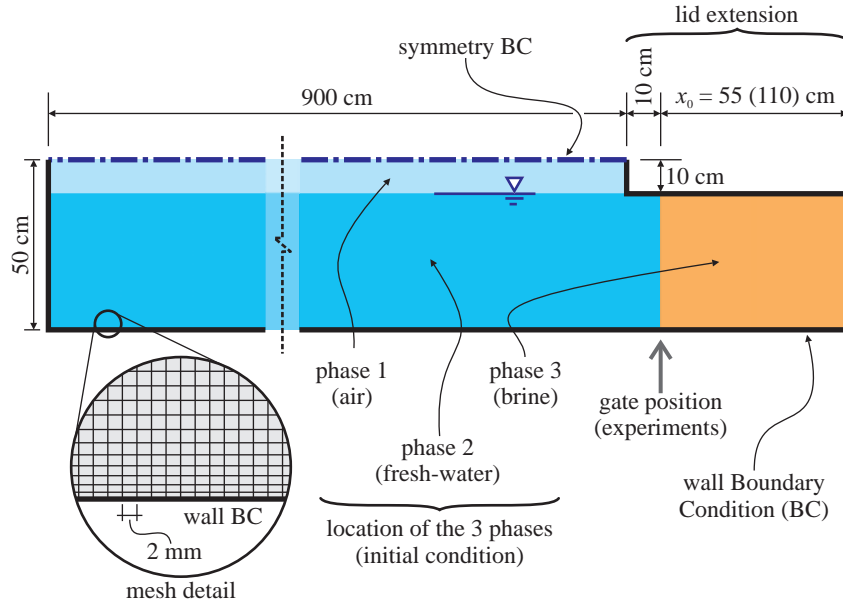
31

Figure A.1: Computational domain, with boundary conditions specification and detailed view of the mesh refinement at the bottom

increased up to 0.002 s.

A.1. Model geometry and computational grid

The experimental apparatus (i.e., the rectangular channel) was modeled in two dimensions at full scale, resulting in a computational domain 9.55 m long (10.10 m in the case of extended lock) and 0.5 m high; see Figure A.1. The domain was discretized by a mesh of more than 1.2×10^6 rectangular cells with a maximum face area of 3.2 mm^2. The minimum cell size was set equal to 1 mm, while the maximum one to 2 mm, with a growing rate of 1.2. The resulting mesh is very regular with a "Minimum Orthogonal Quality" equal to 0.73 ("Orthogonal Quality" ranges from 0 to 1, where values close to 0 correspond to low quality). Finer resolutions of the mesh have been tested without experiencing significant variations in the final results. Figure A.1 also shows a detail of the mesh close to the bottom of the channel.

The no-slip boundary condition was imposed at the bottom and at the sides (i.e., upstream and downstream walls of the channel). The lid which extends over the lock region was also reproduced by an horizontal wall without slip, while the top of the channel was modeled with a symmetry boundary condition (zero normal derivatives). In the numerical model no gate was

necessary and the initial condition was imposed defining the desired value of all the variables in the nodes (e.g., the volume fraction of each phase).

A.2. Some comparisons

Figure A.2 shows a comparison of the velocity field computed with the numerical simulation and measured with the UVP. Figure A.2*a* shows the direct result from the code, while Figure A.2*b* was obtained by using the data resulting from the numerical code sampled with the same pattern of the UVP array of probes, and then applying the "frozen" current hypothesis. Figure A.2*c* shows the velocity field as measured with the UVP and then reproduced under the hypothesis of "frozen" current. We preliminarily note that the main differences between the results shown in Figures A.2*a*-A.2*b* is the absence of the billows effects in the latter. There are also some differences in the nose velocity field, but they are not so relevant, hence the hypothesis of "frozen" current can be adopted with confidence, in particular during the slumping phase when the hypothesis of stationarity holds.

Upon comparing measured velocities with computed velocities, different patterns are evident, with large velocity values appearing in the tail and a more flattened nose.

To extend the comparison to the free surface behaviour, the numerical model was applied with the same conditions of some experiments listed in Table 1. Figure A.3 shows the comparison between the experimental depression and the numerical model for Expt 4 at two different times. The early time profile shows a good agreement with the experiments. The agreement is less good for subsequent times. In particular, the length of the depressed profile is well reproduced. A comparison is also available for the experiments with the lid, where the pressure measured by the differential manometer has been converted into height of ambient fluid column. Figure A.4*a* shows the experimental depression compared to the results of the CFD simulation. The CFD simulation overestimates the experimental value but correctly reproduces the instant of maximum depression and the shape of the height (pressure) time series. Figure A.4*b* shows the measured depression as a function of the front position. The maximum depression lags the front of the current.

The evolution of the nose of the current is shown in Figure A.5, where four snapshots are shown at $t = 5, 10, 15, 20$ s for Expt C16bis. The initial complex structure of the intruding current, with billows swept by the return flow current, progressively evolves toward a simple structure more adherent
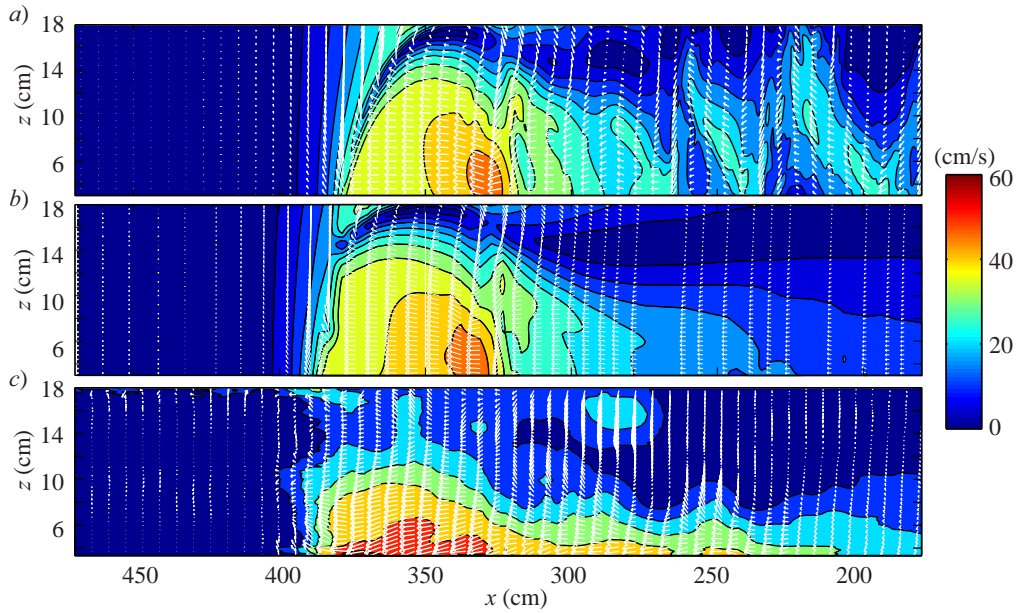
33

Figure A.2: Experiment 9, $r = 0.868$, full-depth. a) Velocity field from numerical simulation; b) velocity field from numerical simulation obtained by applying the "frozen" current hypothesis; c) measurements from UVP under the hypothesis of "frozen" current.
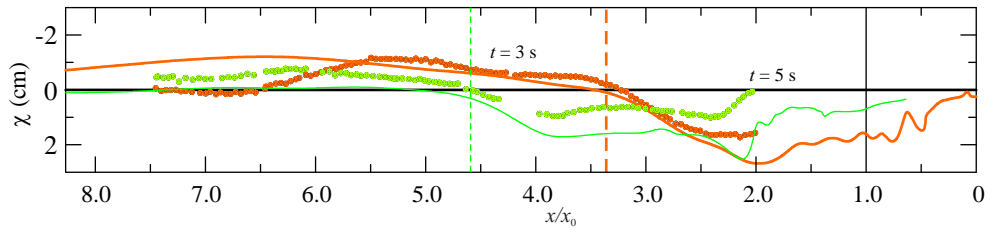

Figure A.3: Depression for Expt 4. The symbols are the experimental data, the continuous lines are the numerical model results. The vertical dashed lines represent the front position at $t = 3$ s (thick dashed line) and $t = 5$ s (thin dashed line).
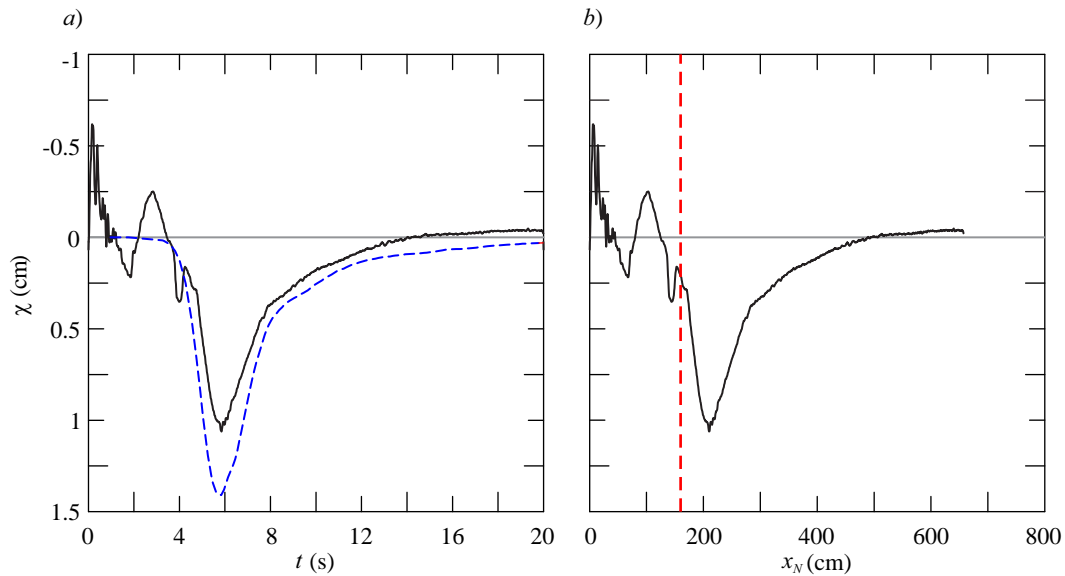
34

Figure A.4: Experiment 9 with a top lid. *a*) Measured (continuous line) and computed (dashed line) pressure virtual-depression at $x = 160$ cm from the gate; *b*) measured depression as a function of the front position. The dashed vertical line indicates the section of measurement of the pressure.

to the scheme of thin GCs. The ambient fluid flow field is also marked by the free surface oscillations, which are dominant in the late stage.

The overall energy balance is shown in Figure A.6. The energy variations, non-dimensional with respect to the potential energy of the current fluid in the lock before release, are shown as a function of the nose position. The kinetic energy increment of the current fluid is accompanied by an increment of the same magnitude also for the ambient fluid, and reaches a maximum (corresponding to the vertical line in the Figure A.6) and then decreases. Most energy is exchanged in potential form between the two fluids, and part of it is dissipated at a constant rate during the slumping phase.
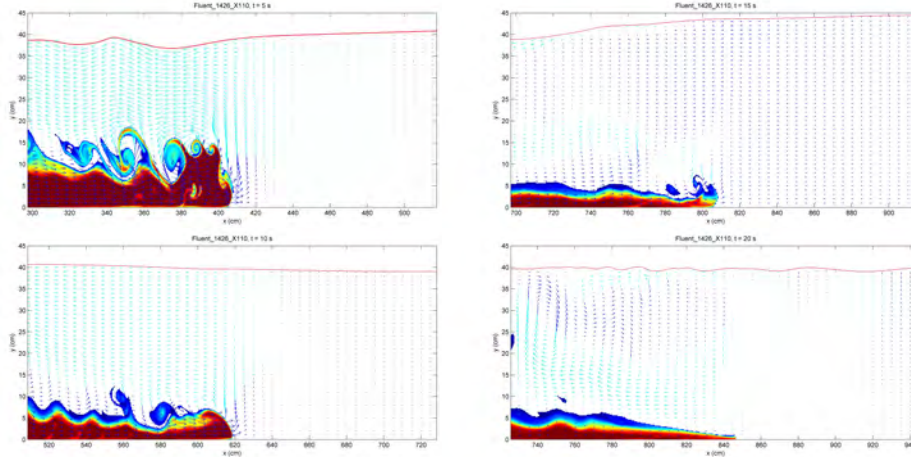
Figure A.5: Snap-shots of the nose ($t = 5, 10, 15, 20$ s) for Expt C16bis, CFD simulation.
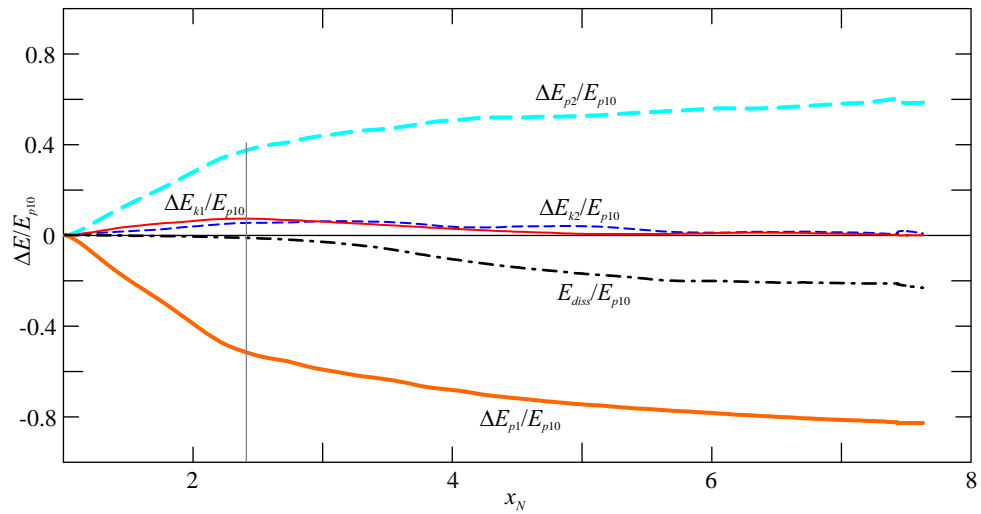

Figure A.6: Energy balance for Expt C16bis, CFD simulation. $\Delta E_{k,p,(1,2)}$ are the variations of kinetic/potential energy for fluid in ambient 1/2, E_{diss} is the dissipated energy. Values are non-dimensionalized with respect to E_{p10}, the potential energy of the intruding fluid in the lock. The vertical line indicates the maximum of kinetic energy of the current fluid.

36

References

[1] T. B. Benjamin, Gravity currents and related phenomena, Journal of Fluid Mechanics 31 (1968) 209–248. doi:10.1017/S0022112068000133.

[2] M. Ungarish, Benjamin's gravity current into an ambient fluid with an open surface, Journal of Fluid Mechanics 825 (2017) 1–11. doi:10.1017/jfm.2017.460.

[3] M. Ungarish, An Introduction to Gravity Currents and Intrusions, Chapman & Hall/CRC Press, Boca Raton London New York, 2009.

[4] H. Gröbelbauer, T. Fanneløp, R. Britter, The propagation of intrusion fronts of high density ratios, Journal of Fluid Mechanics 250 (1993) 669–687. doi:10.1017/S0022112093001612.

[5] R. J. Lowe, J. W. Rottman, P. F. Linden, The non-Boussinesq lock exchange problem. Part 1: Theory and experiments, Journal of Fluid Mechanics 537 (2005) 101–124. doi:10.1017/S0022112005005069.

[6] M. Jacobson, F. Testik, On the concentration structure of high-concentration constant-volume fluid mud gravity currents, Physics of Fluids 25 (1) (2013) 016602. doi:10.1063/1.4774045.

[7] V. Birman, J. Martin, E. Meiburg, The non-Boussinesq lock-exchange problem. Part 2. High-resolution simulations, Journal of Fluid Mechanics 537 (2005) 125–144. doi:10.1017/S0022112093001612.

[8] J. Étienne, E. J. Hopfinger, P. Saramito, Numerical simulations of high density ratio lock-exchange flows, Physics of Fluids 17 (3) (2005) 036601. doi:10.1063/1.1849800.

[9] M. Ungarish, A shallow-water model for high-reynolds-number gravity currents for a wide range of density differences and fractional depths, Journal of Fluid Mechanics 579 (2007) 373–382. doi:10.1017/S0022112007005484.

[10] T. Bonometti, S. Balachandar, J. Magnaudet, Wall effects in non-Boussinesq density currents, Journal of Fluid Mechanics 616 (2008) 445–475. doi:10.1017/S002211200800414X.

[11] M. Ungarish, Two-layer shallow-water dam-break solutions for non-Boussinesq gravity currents in a wide range of fractional depth, Journal of Fluid Mechanics 675 (2011) 27–59. doi:10.1017/S0022112010006397.

[12] T. Bonometti, M. Ungarish, S. Balachandar, A numerical investigation of constant-volume non-Boussinesq gravity currents in deep ambient, Journal of Fluid Mechanics 673 (2011) 574–602. doi:10.1017/S0022112010006506.

[13] R. Rotunno, J. B. Klemp, G. H. Bryan, D. J. Muraki, Models of non-Boussinesq lock-exchange flow, Journal of Fluid Mechanics 675 (2011) 1–26. doi:10.1017/jfm.2010.648.

[14] B. Turnbull, J. McElwaine, Experiments on the non-Boussinesq flow of self-igniting suspension currents on a steep open slope, Journal of Geophysical Research: Earth Surface 113 (F1). doi:10.1029/2007JF000753.

[15] A. Dai, Non-Boussinesq gravity currents propagating on different bottom slopes, Journal of Fluid Mechanics 741 (2014) 658–680. doi:10.1017/jfm.2014.5.

[16] T. O. Robinson, I. Eames, R. Simons, Dense gravity currents moving beneath progressive free-surface water waves, Journal of Fluid Mechanics 725 (2013) 588–610. doi:10.1017/jfm.2013.112.

[17] L. Stancanelli, R. Musumeci, E. Foti, Dynamics of gravity currents in the presence of surface waves, Journal of Geophysical Research: Oceans 123 (3) (2018) 2254–2273. doi:10.1002/2017JC013273.

[18] S. M. Taghavi, T. Seon, D. M. Martinez, I. A. Frigaard, Influence of an imposed flow on the stability of a gravity current in a near horizontal duct, Physics of Fluids 22 (3) (2010) 031702. doi:10.1063/1.3326074.

[19] S. Longo, M. Ungarish, V. Di Federico, L. Chiapponi, F. Addona, Gravity currents produced by constant and time varying inflow in a circular cross-section channel: Experiments and theory, Advances in Water Resources 90 (2016) 10 – 23. doi:10.1016/j.advwatres.2016.01.011.

[20] G. Sciortino, C. Adduce, V. Lombardi, A new front condition for non-Boussinesq gravity currents, Journal of Hydraulic Research (2018) 1–9doi:10.1080/00221686.2017.1395371.

[21] C. Adduce, G. Sciortino, S. Proietti, Gravity currents produced by lock exchanges: experiments and simulations with a two-layer shallow-water model with entrainment, Journal of Hydraulic Engineering 138 (2) (2011) 111–121. doi:10.1061/(ASCE)HY.1943-7900.0000484.

[22] S. Longo, Experiments on turbulence beneath a free surface in a stationary field generated by a crump weir: free-surface characteristics and the relevant scales, Experiments in Fluids 49 (6) (2010) 1325–1338. doi:10.1007/s00348-010-0881-5.

[23] S. Longo, Experiments on turbulence beneath a free surface in a stationary field generated by a crump weir: turbulence structure and correlation with the free surface, Experiments in Fluids 50 (1) (2011) 201–215. doi:10.1007/s00348-010-0921-1.

[24] H. Nakagawa, I. Nezu, Structure of space-time correlations of bursting phenomena in an open-channel flow, Journal of Fluid Mechanics 104 (1981) 1–43. doi:10.1017/S0022112081002796.

[25] K. W. Morton, D. F. Mayers, Numerical solution of partial differential equations: an introduction, Cambridge University Press, 1994.

[26] ANSYS, ANSYS Academic Research CFD.

[27] J. O. Shin, S. B. Dalziel, P. F. Linden, Gravity currents produced by lock exchange, Journal of Fluid Mechanics 521 (2004) 1–34. doi:10.1017/S002211200400165X.